Characterizing the Lipkin-Meshkov-Glick excited-state spectrum through the quantum coherence spectrum

Qian Wang [*]
Department of Physics, Zhejiang Normal University, Jinhua, Zhejiang 321004, China
and Center for Applied Mathematics and Theoretical Physics, University of Maribor, Mladinska 3, 2000 Maribor, Slovenia

Jamil Khalouf-Rivera
Departamento de Ciencias Integradas y Centro de Estudios Avanzados en Física, Matemáticas y Computación, Universidad de Huelva, Huelva 21071, Spain

Francisco Pérez-Bernal [†]
Departamento de Ciencias Integradas y Centro de Estudios Avanzados en Física, Matemáticas y Computación, Universidad de Huelva, Huelva 21071, Spain
and Instituto Carlos I de Física Teórica y Computacional, Universidad de Granada, Granada 18071, Spain

(Received 25 September 2024; accepted 3 March 2025; published 11 March 2025)

Excited-state quantum phase transitions extend the quantum phase transition concept beyond the ground state and offer insights into the complex behavior of quantum systems. In the present work we assess the use of the multiple quantum coherence spectrum as a valid tool to probe excited-state quantum phase transitions within the framework of the Lipkin-Meshkov-Glick model. The time dependence and the long-time average of the multiple quantum coherence spectrum reveal the intricate dynamics that stems from the existence of singularities in the excited-state spectrum of a quantum many-body system.

DOI: 10.1103/PhysRevA.111.032209

I. INTRODUCTION

Quantum phase transitions, also known as ground-state quantum phase transitions (GSQPTs), are nonthermal phase transitions characterized by abrupt changes in the ground state of a quantum system once one or more Hamiltonian control parameters reach certain critical values [1,2]. This concept was expanded to encompass excited states, which leads to the definition of excited-state quantum phase transitions (ESQPTs) [3–5]. For a recent review on the subject see Ref. [6]. Unlike GSQPTs, which convey nonanalytical changes in the ground-state properties of the system, ESQPTs are associated with nonanalyticities in the level flow and density of states (DOS) of the system in its mean-field or large-system-size limit [6,7]. ESQPTs are found in various many-body quantum systems, e.g., the Lipkin-Meshkov-Glick (LMG) model [8–13], the Dicke and Rabi models [14–19], spinor Bose-Einstein condensates [20–22], ferromagnetic quantum gases [23], the vibron model [24–30], periodically driven systems [31,32], the interacting boson model [33,34], the coupled top model [35,36], and Kerr nonlinear oscillators [37–40].

The nonanalytical effects associated with ESQPTs have clear precursors at finite system sizes that modify the structure and dynamics of the system. The presence of an ESQPT is usually revealed in the closing of the gap between adjacent energy levels, the appearance of exceptional points, or extremal values of quantities such as the order parameter of the associated GSQPT, the participation ratio, or the quantum fidelity susceptibility [10,13,27,29,41]. Thermal properties of systems with a finite number of degrees of freedom can also be strongly modified due to the existence of an ESQPT with anomalous thermal relaxation or the presence of a singularity in the microcanonical heat capacity in the vicinity of the ESQPT critical energy [42,43]. Finally, ESQPTs can also have a strong impact on system dynamics as revealed in the study of the system under sudden quantum quenches, with strong effects on the survival probability of the initial state and a maximally enhanced decoherence; in the study of the time dependence of out-of-time-order correlators (OTOCs), where the enhanced information scrambling associated with the unstable character of the ESQPT critical energy is revealed; and in peculiar features in nonequilibrium thermodynamics [11,15,38,44–52]. Recently, ESQPT precursors have also been identified in dissipating systems, modeled by complex-valued Hamiltonians [53,54].

Quantum coherence is one of the cornerstones of quantum theory and it plays an important role in various quantum technologies [55]. For any given basis, a pure quantum state

[*]Contact author: qwang@zjnu.edu.cn
[†]Contact author: curropb@uhu.es

can be expressed using its density matrix, emphasizing the concept of probability distribution in the quantum formalism and removing the arbitrary overall phase that is implicit when expressing quantum states as vectors in a Hilbert space. The diagonal elements of the density matrix are known as populations or the zeroth order of the multiple quantum coherence (MQC) spectrum, while nondiagonal elements are referred to as coherences or the nth order of the MQC spectrum, with n depending on the order of nondiagonal in the density matrix. Nonzero coherences in a pure quantum state density matrix imply that the corresponding elements of the selected basis are in a quantum superposition, introducing quantum interference effects. Since its introduction in nuclear magnetic resonance studies [56–58], the MQC spectrum has proved a valuable tool with different applications. It gives access to many-body quantum coherences [56,59,60] and to the evolution of correlations [61,62] and entanglement [63–65]. Beyond the usual experimental access to MQC spectra in nuclear magnetic resonance studies, recent advances in cold-atom physics (ion traps, ultracold atoms, or Bose-Einstein condensates) paved the way to the access to MQC spectra for pure quantum states at temperatures close to zero. In particular, Gärttner *et al.* measured the MQC spectrum using a trapped-ion setup [66], demonstrating the link between MQC spectra and OTOCs and suggesting an experimentally feasible MQC protocol that provides access to multiparticle entanglement through quantum Fisher information [67].

The MQC spectrum is also a valid probe to detect GSQPTs in Hermitian [68,69] and non-Hermitian systems [70], as well as the transition to localization in disordered systems [71–73]. In this article we investigate how the existence of an ESQPT in the LMG model modifies quantum coherence and whether the MQC spectrum is a valid probe for ESQPTs.

The LMG model was first introduced in nuclear physics to describe interacting fermions with a toy model, simple enough to be solved exactly, which could be used to validate different approximations [74–76]. Despite its simplicity, it was revealed to be a versatile model, with enough physical content to be used in other disciplines. It has proved a convenient platform for studies on quantum phase transitions [5,6,8,77–83], quantum thermodynamics [52,84–87], quantum metrology [88–90], quantum control [91–93], and quantum information [94–99]. It has also been employed to explore the influence of unstable stationary points on the spreading of OTOCs [100,101], the behavior of the complexity in a system with infinite-range interaction [102], the existence of Floquet time crystals in a system without disorder [103], and the link between the critical phenomena of static Hamiltonians and the features observed in periodic quenched systems [104]. A very positive aspect of this model is that it can be accomplished in a variety of experimental platforms [105–116].

The LMG model Hamiltonian in the present paper undergoes a second-order GSQPT and an associated ESQPT in the GSQPT broken-symmetry phase, which is characterized by a logarithmic divergence of the DOS at the critical energy [7]. Such divergence is a consequence of an unstable fixed point appearing in the dynamics of the classical limit of the model. We show that the occurrence of the ESQPT leads to a drastic change in the MQC spectrum for time-evolved and long-time-averaged states. We also illustrate how to identify ESQPT signatures from the behavior of the MQC spectrum zero mode and we demonstrate that the MQC spectrum width is a reliable ESQPT probe. Thus, the aim of the present paper is to provide a detailed exploration of the interplay between an ESQPT and the MQC spectrum and to evince the usefulness of the MQC spectrum as an ESQPT detector in many-body quantum systems.

The article is structured as follows. In Sec. II we begin with a brief review of the concept of the MQC spectrum. In Sec. III we present the LMG model and its classical limit, emphasizing the main features of the model ESQPT. Our main results are given in Sec. IV. In Sec. IV A we discuss the time dependence of the MQC spectrum of a state once the system undergoes a quantum quench. In Sec. IV B we study how the MQC spectrum width is a valid ESQPT probe. In Sec. IV C we provide a study of the MQC spectrum for the resulting long-time-averaged state after the quench. We summarize our results and discuss conclusions in Sec. V.

II. MULTIPLE QUANTUM COHERENCE PROTOCOL

The MQC protocol, initially introduced in nuclear magnetic resonance studies [56,117,118], provides information about multiparticle quantum coherences, the nondiagonal elements of the density matrix. Let us consider a Hermitian operator $\hat{\mathcal{O}}$, with real eigenvalues ν_n and associated eigenstates $|\nu_n\rangle$. The density matrix of an arbitrary pure quantum state ρ can be expressed in the $\{|\nu_n\rangle\}$ basis as

$$\rho = \sum_{\ell} \rho_\ell = \sum_{\ell} \sum_{\nu_n - \nu_m = \ell} \rho_{nm} |\nu_n\rangle\langle\nu_m|, \tag{1}$$

where $\rho_{nm} = \langle\nu_n|\rho|\nu_m\rangle$ and the index ℓ takes all possible values determined by the $\nu_n - \nu_m$ differences. Each ρ_ℓ block is known as an ℓ coherence and it contains information about coherences between eigenstates of $\hat{\mathcal{O}}$ whose eigenvalues differ by ℓ, $\nu_n - \nu_m = \ell$. The ℓth multiple quantum intensity $I_\ell(\rho)$ is defined as the square of the Frobenius norm (also known as the Hilbert-Schmidt norm or Schatten 2-norm) of ρ_ℓ [67,68,70],

$$I_\ell(\rho) \equiv (\|\rho_\ell\|_2)^2 = \mathrm{Tr}(\rho_\ell^\dagger \rho_\ell). \tag{2}$$

The set of all $I_\ell(\rho)$ intensities forms the ρ state MQC spectrum. Note that the sum of the multiple quantum intensities over all possible ℓ values is 1 if and only if ρ is a pure quantum state. Apart from the information about coherences of the system provided by the $\ell \neq 0$ intensities, the $\ell = 0$ intensity depends on the density-matrix populations, the diagonal matrix elements of the density matrix.

As shown in Refs. [66,67,119], multiple quantum intensities can be experimentally accessed through a protocol defined in three steps. A given initial pure quantum state $\hat{\rho}_i$ is evolved for a time t under a nontrivial Hamiltonian resulting in $\hat{\rho}_t = \hat{U}(t)\hat{\rho}_i\hat{U}^\dagger(t)$, where $\hat{U}(t) = e^{-i\hat{H}t}$. This is followed by the application of the operator $\hat{W}(\phi) = e^{-i\hat{\mathcal{O}}\phi}$ and a backward evolution of time $-t$ producing the final state $\hat{\rho}_f$. It can be shown that the fidelity $F_t(\phi) = \mathrm{Tr}[\hat{\rho}_i\hat{\rho}_f(\phi)]$, using cyclic

permutations under the trace, is expressed as

$$F_t(\phi) = \mathrm{Tr}[\hat{\rho}_i \hat{\rho}_f(\phi)] = \mathrm{Tr}[\hat{\rho}_t \hat{\rho}_t(\phi)] = \sum_\ell I_\ell e^{-i\ell\phi}, \qquad (3)$$

where $\hat{\rho}_t(\phi) = \hat{W}(\phi)\hat{\rho}_t\hat{W}^\dagger(\phi)$. From Eq. (3) it is clear that the Fourier transform of the fidelity with respect to ϕ gives access to the values of the different multiple quantum intensities. Another point developed in Refs. [66,67,119] is the connection of the MQC spectrum to an OTOC. Given two operators $\hat{V}$ and $\hat{W}$ and an initial state, an OTOC measures the spread in time of the operator $\hat{W}$ through the expectation value of the commutator squared module $\langle[\hat{W}_t, \hat{V}]^\dagger[\hat{W}_t\hat{V}]\rangle$, where $\hat{W}_t = e^{i\hat{H}t}\hat{W}e^{-i\hat{H}t}$. This commutator has a term equal to a time-disordered matrix element of the operators in the given initial state $F_{\hat{V},\hat{W}}(t) = \langle\hat{W}_t^\dagger\hat{V}^\dagger\hat{W}_t\hat{V}\rangle$. In the MQC case one can define $\hat{V}$ as the initial matrix density $\hat{\rho}_i$ and $\hat{W}$ as the $\hat{W}(\phi)$ operator, which for the case of small ϕ values can be shown to be a fidelity OTOC (FOTOC) [119].

Out-of-time order correlators are sensitive to the sudden changes in the ground state associated with GSQPTs [120], and the equivalence between MQC spectra and OTOCs indicates the MQC's suitability to detect and characterize such transitions, as demonstrated in Refs. [68,69]. Out-of-time order correlators have also proved useful in the detection and study of ESQPTs [46]. In the present article our aim is to characterize the LMG model ESQPT making use of the MQC spectrum and its second moment

$$\Sigma(\rho, \hat{\mathcal{O}}) = \left(\sum_\ell \ell^2 I_\ell(\rho)\right)^{1/2}, \qquad (4)$$

a quantity that recently has been proved to be equal to the quantum Fisher information for pure quantum states [67].

III. LIPKIN-MESHKOV-GLICK MODEL

The LMG model has different mathematical realizations. Nowadays, the most frequently used one is a fully connected Ising model, a spin-1/2 chain with N elements and all-to-all infinite-range interactions. The Pauli matrix of the ith spin along the α axis is $\hat{\sigma}_i^\alpha$, with $\alpha = x, y, z$ and $i = 1, \ldots, N$. Considering collective quasispin operators $\hat{J}_\alpha = \sum_{i=1}^N \hat{\sigma}_i^\alpha/2$, the spin-chain Hamiltonian can be recast as a simpler collective Hamiltonian with a second-order GSQPT and an associated ESQPT

$$\hat{H} = \varepsilon\left[-\frac{2\kappa}{N}\hat{J}_x^2 + (1-\kappa)\left(\hat{J}_z + \frac{N}{2}\right)\right], \qquad (5)$$

with a control parameter κ defined in the $0 \leqslant \kappa \leqslant 1$ range. Here and throughout the present work we set $\hbar = 1$ and the energy scale $\varepsilon = 1$, making the Hamiltonian dimensionless. The Hamiltonian (5) conserves the total number of particles N. The use of collective quasispin operators implies a drastic reduction of the Hilbert space dimension, from a total dimension of 2^N in the spin-chain case to $N+1$ if we only consider the totally symmetric representation spanned by Dicke states (symmetric states with all spins coupled to the maximum quasispin value $j = N/2$). There exists an additional $\mathbb{Z}_2$ symmetry in the Hamiltonian (5), the parity symmetry $\hat{\Pi} = e^{i\pi(j+\hat{J}_z)}$, that divides the Hilbert space into even and odd nonmixing blocks. Hence, we can restrict our study to the even-parity block, reducing further the Hilbert space dimension to $(N - N \bmod 2)/2 + 1$. The Hamiltonian (5) can be diagonalized in the Dicke basis $|m\rangle$ defined as $J_z|m\rangle = m|m\rangle$, where $-j \leqslant m \leqslant j$, splitting the basis into two subsets according to the parity of the quantum number m.

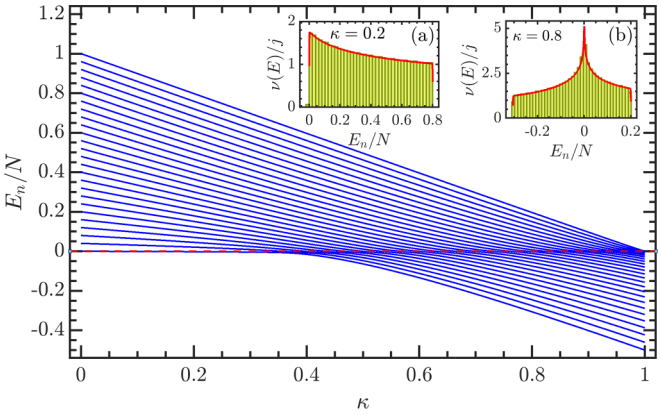

FIG. 1. Normalized energy spectrum of the Hamiltonian (5) as a function of the control parameter κ with $j = N/2 = 25$. The dashed horizontal line marks the critical ESQPT energy $E_c = 0$. The scaled density of states is depicted in the two insets, for a κ value less than κ_c [$\kappa = 0.2$ in inset (a)] and a value larger than the critical one [$\kappa = 0.8$ in inset (b)] for a system size $N = 5000$. The red solid line in each inset is the classical limit result $\nu_c(E)$ from Eq. (13) (see the text for details). The ESQPT in the model is characterized by a divergence in the level density $\nu(E)$, as shown in inset (b). All plotted quantities are dimensionless.

The ground state of the Hamiltonian (5) undergoes a second-order GSQPT at the control parameter critical value $\kappa_c = 1/3$, which separates the symmetric phase $\kappa < \kappa_c$, also known as the normal or ferromagnetic phase, from the broken-symmetry phase $\kappa > \kappa_c$, often called superradiant or paramagnetic phase. The signatures of this GSQPT have been thoroughly investigated in the literature [8,80–84,121–123]. It is also known that the Hamiltonian (5) exhibits an ESQPT for $\kappa > \kappa_c$, with a critical energy $E_c = 0$ [5,6,11,13,124]. In this work we characterize the LMG ESQPT using an MQC protocol.

Excited-state quantum phase transitions are characterized by a nonanalytic density of states at a certain excitation energy, the ESQPT critical energy [5–7]. In Fig. 1 we show the correlation energy diagram for the Hamiltonian (5) as a function of the control parameter κ for a system with size $N = 50$. A high-density-of-states line can be appreciated at the normalized energy $E_c/N = 0$. In the insets of Fig. 1, we show the density of states, defined as $\nu(E) = \sum_n \delta(E - E_n)$, for $\kappa = 0.2 < \kappa_c$ in inset (a) and $\kappa = 0.8 > \kappa_c$ in inset (b). The green bars have been numerically computed for a system with a size $N = 5000$, while the red solid line is the result obtained in the mean-field limit of the system as we explain below. There is a clear contrast between the $\kappa < \kappa_c$ results, with no ESQPT, and the high density of levels around $E_c/N = 0$ for $\kappa > \kappa_c$ [11,12,41,124], which develops into a logarithmic divergence at the classical limit [6,7].

The ESQPT in the LMG model can be understood by considering the stationary points of the classical limit of the system, obtained for $N \to \infty$ [6], using quasispin coherent states [125,126]

$$|\xi\rangle = \frac{1}{(1+|\xi|^2)^j} e^{\xi \hat{J}_+} |j, -j\rangle, \tag{6}$$

where $\xi \in \mathbb{C}$ is a variational parameter and $\hat{J}_\pm = \hat{J}_x \pm i\hat{J}_y$ are quasispin raising and lowering operators. The expectation value of the operators needed to study the Hamiltonian (5) are [125]

$$\begin{aligned}\langle \xi|\hat{J}_+|\xi\rangle &= \frac{2j\xi^*}{1+|\xi|^2},\\ \langle \xi|\hat{J}_-|\xi\rangle &= \frac{2j\xi}{1+|\xi|^2},\\ \langle \xi|\hat{J}_z|\xi\rangle &= j\left(\frac{|\xi|^2-1}{|\xi|^2+1}\right).\end{aligned} \tag{7}$$

Taking this into account, the classical limit of the Hamiltonian (5) is

$$\begin{aligned}\mathcal{H}_c(\xi) &= \frac{\langle \xi|\hat{H}|\xi\rangle}{N}\\ &= -\frac{\kappa(\xi+\xi^*)^2}{2(1+|\xi|^2)^2} + (1-\kappa)\frac{|\xi|^2}{1+|\xi|^2}.\end{aligned} \tag{8}$$

The complex parameter ξ can be mapped into classical canonical variables (p, q), considering the change of variables

$$\xi = \frac{q+ip}{\sqrt{4-(p^2+q^2)}}, \tag{9}$$

and Eq. (8) transforms to the classical limit of the LMG Hamiltonian (5)

$$\mathcal{H}_c(p,q) = -\frac{\kappa q^2}{8}(4-p^2-q^2) + \frac{1-\kappa}{4}(p^2+q^2). \tag{10}$$

The $(q, p)_s$ stationary points of $\mathcal{H}_c(p, q)$ are the solutions of $\nabla\mathcal{H}_c(p, q) = 0$,

$$(q,p)_s = \begin{cases}(0,0) & \text{for } \kappa \leqslant \kappa_c\\ \left(\pm\sqrt{\frac{3\kappa-1}{\kappa}}, 0\right) & \text{for } \kappa > \kappa_c.\end{cases} \tag{11}$$

Note that for $\kappa \leqslant \kappa_c$ there is a single stationary point, a minimum at the origin $(q, p)_s = (0, 0)$. For control parameter values $\kappa > \kappa_c$, the stationary point in the origin is a saddle point and two identical minima appear at zero momentum $(q, p)_s = \sqrt{(\pm\frac{3\kappa-1}{\kappa}, 0)}$. The ground-state energy functional in the mean-field limit can be obtained by calculating the value of the classical Hamiltonian (10) evaluated in the corresponding global minimum

$$\mathcal{E}_{gs}(\kappa) = \begin{cases}0 & \text{for } \kappa \leqslant \kappa_c\\ -\frac{(3\kappa-1)^2}{8\kappa} & \text{for } \kappa > \kappa_c.\end{cases} \tag{12}$$

It can be easily shown that the second derivative of the energy functional (12) with respect to the control parameter is discontinuous when evaluated at the critical value of the control parameter, as expected in a second-order GSQPT [122].

Figure 2 depicts energy contour plots of the classical limit of the LMG model in Eq. (10) for three different values of κ.

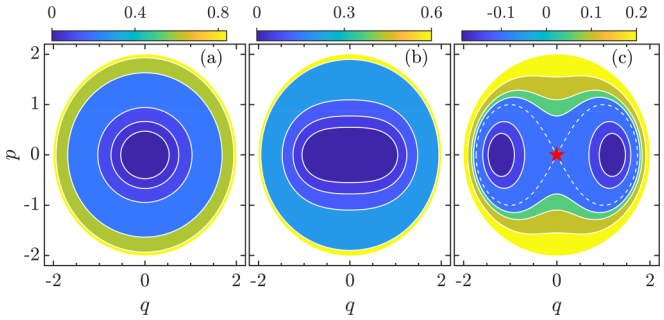

FIG. 2. Energy surface contour plots for the classical Hamiltonian (10) with control parameter values (a) $\kappa = 0.3\kappa_c$, (b) $\kappa = \kappa_c$, and (c) $\kappa = 2\kappa_c$. The red star and the dashed line in (c) denote the saddle point and its corresponding energy separatrix in phase space, respectively. This unstable critical point in the classical limit of the LMG model is associated with the ESQPT in the quantum system. The critical control parameter value is $\kappa_c = 1/3$. All quantities are dimensionless.

In Fig. 2(a) we observe that, as mentioned above, for $\kappa < \kappa_c$ the energy surface has a global minimum at the origin (0,0). At $\kappa = \kappa_c$ [Fig. 2(b)] the system exhibits a flatter minimum (quartic order) that splits into two symmetric wells for values of $\kappa > \kappa_c$ [Fig. 2(c)].

For a fixed value of the control parameter, the available phase-space volume depends on the energy

$$\nu(E) = \frac{1}{2\pi}\iint \delta(E - \mathcal{H}_c(p,q))dp\,dq. \tag{13}$$

Note that $\nu(E)$ is the smooth component in the Gutzwiller trace formula [127], identified as the semiclassical approximation to the quantum density of states [5,12,14].

Following the approach outlined in Refs. [12,14], we plot $\nu(E)$ for two different values of κ in the insets of Fig. 1 using red solid lines. The agreement between $\nu(E)$ and the numerical results (green bars) computed for a system with $N = 5000$ is excellent. Furthermore, in the broken-symmetry phase, the DOS exhibits a logarithmic divergence at the normalized critical energy $E_c/N = 0$ due to the saddle point of the classical energy surface [see the red star in Fig. 2(c)] [5,12].

IV. RESULTS

To demonstrate the convenience of the MQC spectrum as a probe of the LMG model ESQPT in the Hamiltonian (5), we consider the following sudden-quench protocol. Initially, the system is prepared in a $|\psi_0\rangle$ state that is the even-parity ground state of an LMG Hamiltonian $\hat{H}_0$, with a κ control parameter value such that the system is in the broken-symmetry phase ($\kappa_c < \kappa < 1$). At $t = 0$, a $\hat{J}_x^2$ interaction with strength $-2\chi/N$ is added to the Hamiltonian, giving rise to a nontrivial time evolution of the initial state governed by the Hamiltonian $\hat{H}_1 = \hat{H}_0 - (2\chi/N)\hat{J}_x^2$. The value of the quench parameter χ allows us to bring the system to different excited-state phases. The critical value of the quench parameter χ_c brings the initial state to the ESQPT critical energy $E_c/N = 0$ and its value can be obtained from the classical approach using the tangent

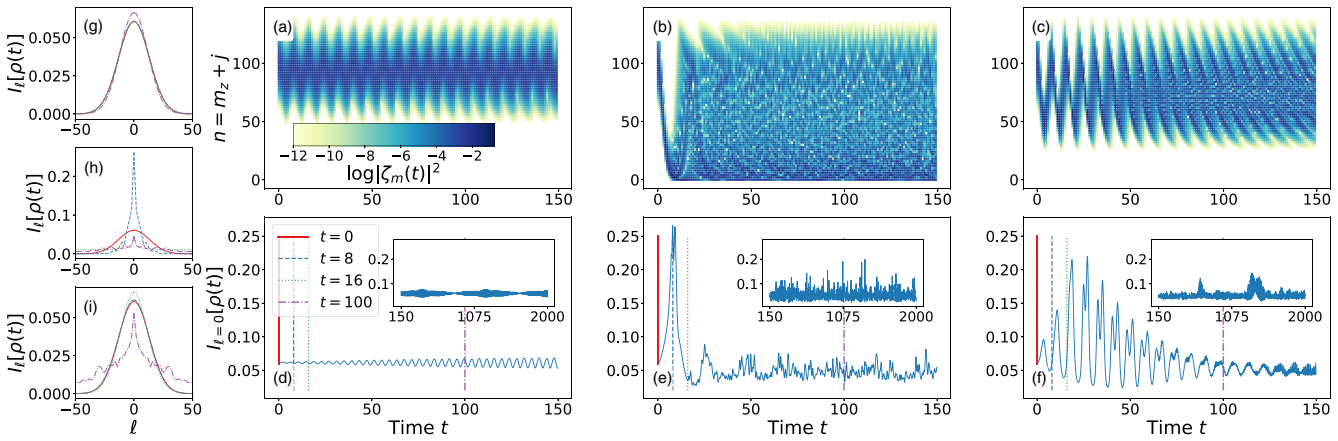

FIG. 3. (a)–(c) Heat maps displaying the coefficients $|\zeta_m(t)|^2$ as a function of the $n = m_z + j$ quantum number (ordinate) and time (abscissas) for (a) $\chi = 0.2\chi_c$, (b) $\chi = \chi_c$, and (c) $\chi = 2\chi_c$ with $\kappa = 1.5\kappa_c$ and system size $N = 400$. (d)–(f) Zeroth-order component of the MQC spectrum $I_0[\rho(t)]$, defined in Eq. (19), as a function of time t. Values of χ, κ, and N are the same as in (a)–(c). The insets display the same quantity in a larger time span. The six plots share the abscissa axis range. (g)–(i) Plot of $I_\ell[\rho(t)]$ versus the differences ℓ for the selected values of time [see the legend in (d)] highlighted in (d)–(f) with vertical dashed lines, using the same color code and line style. The large spreading of $|\zeta_m(t)|^2$ and its rapid decay to $n = 0$ value in (b) and the particular evolution of $I_0[\rho(t)]$ in (e) are dynamical signatures of the LMG model ESQPT. The other parameters are $\kappa_c = 1/3$ and χ_c given by Eq. (14).

method [15,49]

$$\chi_c = -\frac{\kappa(3\kappa - 1)}{\kappa + 1}, \tag{14}$$

with $\kappa_c < \kappa < 1$. We would like to emphasize that the ESQPT for the LMG model Hamiltonian (5) only exists in the broken-symmetry phase, for control parameter values in the range $\kappa_c < \kappa < 1$. As we pay attention to the ESQPT imprints in the MQC spectrum, the present study is restricted to the broken-symmetry phase.

A. Quenched-state MQC spectrum

We first calculate the MQC spectrum of the state at a time t after the quench

$$\rho(t) = |\psi_t\rangle\langle\psi_t| = e^{-iH_1 t}\rho(0)e^{iH_1 t}, \tag{15}$$

where $\rho(0) = |\psi_0\rangle\langle\psi_0|$ is the density matrix of the initial state of the system. We compute the MQC spectrum with $\hat{\mathcal{O}} = \hat{J}_z$. The decomposition of $\rho(t)$ in the eigenbasis of $\hat{J}_z$, $\{|m\rangle\}_{m=-j}^{m=j}$, is

$$\rho(t) = \sum_\ell \rho_\ell(t) = \sum_{\ell=-2j}^{2j} \sum_m \rho_{m+\ell,m}(t)|m+\ell\rangle\langle m|, \tag{16}$$

where the m index in the sum is such that $|m + \ell| \leqslant j$ and

$$\begin{aligned}\rho_{m+\ell,m}(t) &= \langle m+\ell|\rho(t)|m\rangle = \langle m+\ell|e^{-i\hat{H}_1 t}|\psi_0\rangle\langle\psi_0|e^{i\hat{H}_1 t}|m\rangle \\ &= \zeta_{m+\ell}(t)\zeta_m^*(t),\end{aligned} \tag{17}$$

with $\zeta_m(t) = \langle m|\psi_0(t)\rangle$ for $m = -j, \ldots, j$. Introducing the closure relation for the $\hat{H}_1$ eigenstates $\{|\phi_k^\alpha\rangle\}$, one can easily prove that $\zeta_m(t) = \sum_{k,\alpha}\langle m|\phi_k^\alpha\rangle\langle\phi_k^\alpha|\psi_0\rangle e^{-iE_k t}$. The eigenstates are such that $\hat{H}_1|\phi_k^\alpha\rangle = E_k|\phi_k^\alpha\rangle$ and the α index is only needed in case there are degenerate states.

The next step is to assess whether the MQC spectrum is a useful tool for ESQPT characterization. With this aim in mind, we plot the time dependence of the $\zeta_m(t)$ factors in Figs. 3(a)–3(c), the population time evolution $I_0(t)$ in Figs. 3(d)–3(f), and the dependence of $I_\ell(t)$ with ℓ for selected time values in Figs. 3(g)–3(i). In all cases, calculations are performed for a system with $\kappa = 0.5$, $N = 400$, and values of the quench parameter χ below, at, and above the critical value $\chi_c = -1/6$.

As mentioned above, the time dependence of $\log|\zeta_m(t)|^2$ is shown as a heat map in Figs. 3(a)–3(c), where we plot $\log|\zeta_m(t)|^2$ [using the color scale introduced in Fig. 3(a)] versus the quantum number $n = m + j$ and time. Values of $|\zeta_m(t)|^2$ less than 10^{-12} have been truncated to zero. In a static problem, the transition state is known to be localized in the ground state of the Hamiltonian $\hat{H}(\kappa = 0)$, i.e., the $n = 0$ basis state [11]. In our case, $\zeta_m(t)$ is the time evolution of the m_z component of $|\psi_0\rangle$. If the initial state remains in the broken-symmetry phase after the quench, the quenched state has large components for the the ground state and the first few excited states of $\hat{H}_1$. As these eigenstates belong to the symmetric phase, they have large components for basis states with large-n values. The resulting dynamics is characterized by regular oscillations of small amplitude in time as shown in Figs. 3(a) and 3(d) for $\chi = 0.2\chi_c$. The results obtained when the quenched state lies in the symmetric phase are similar to the previous ones, although the time evolution of $|\psi_0(t)\rangle$ is now dependent on eigenstates of $\hat{H}_1$ with energies above the ESQPT critical energy, with an energy dependence that is more complex than in the symmetric case and with a wider distribution width in the $\hat{J}_z$ basis states. This leads to an evolution of $|\zeta_m(t)|^2$ with slightly larger amplitudes and more irregular oscillations for long times, as can be appreciated in Figs. 3(c) and 3(f) for $\chi = 2\chi_c$. Finally, if $\chi = \chi_c$, the quench brings the system to the ESQPT critical energy. The results for this critical case are shown in Figs. 3(b) and 3(e), where the $|\psi_0(t)\rangle$ state gets rapidly localized in the $n = 0$ basis state, the ground state of $\hat{J}_z$. The rapid localization can be explained from the divergence in the density of states, which makes the

eigenstates with energies close to the critical value dominate the dynamics of the system at the initial time. The highly localization feature of these eigenstates, originally explained in [11,41], can be explained in an intuitive manner considering that the critical ESQPT energy is associated with a unstable stationary point (a saddle point) in the classical limit, which favors the localization in the $n = 0$ state as the quantum system should have a large probability of localization in the origin. The initial localization observed in the evolution of $|\psi_0(t)\rangle$ can be explained in this way, as well as the unstable dynamics at the critical energy of the ESQPT, with a fast spread of $|\psi_0(t)\rangle$ in the eigenstates of $\hat{H}_1$. Therefore, the evolution is such that the time-evolved state is delocalized in more basis states than in the pre- or postcritical energy quench cases, even though $|\psi_0(t)\rangle$ remains localized in the $n = 0$ basis state, an apparent conundrum already discussed in [38]. The unstable dynamics when the quenched state straddles the critical ESQPT energy is consistent with the results obtained in Refs. [46,49,100,101] and supports our initial assumption of considering the MQC spectrum and its width a valid probe for ESQPTs. We carry out a detailed comparison of the dynamical features of the MQC spectrum width and FOTOC in the following section.

Taking into consideration the MQC intensity definition in Eq. (2), the ℓth MQC intensity of $\rho(t)$ is given by

$$I_\ell[\rho(t)] = \mathrm{Tr}[\rho_\ell^\dagger(t)\rho_\ell(t)] = \sum_m |\zeta_m(t)|^2 |\zeta_{m+\ell}(t)|^2. \quad (18)$$

Therefore, the MQC intensities $\{I_\ell[\rho(t)]\}_{\ell=-2j}^{\ell=2j}$ depend on $|\zeta_m(t)|^2$ for $m = -j, \ldots, j$. The maximal MQC intensity corresponds to the population intensity

$$I_0[\rho(t)] = \sum_m |\zeta_m(t)|^4, \quad (19)$$

which is a time-dependent inverse participation ratio (IPR) that measures the localization of the evolved state $|\psi(t)\rangle$ in the $\hat{J}_z$ basis. In Figs. 3(d)–3(f) we show $I_0(t)$ for the same quench parameter values selected in Figs. 3(a)–3(c). The depicted $I_0(t)$ results can be understood by considering that $I_0(t)$ is an IPR and our previous discussion of the results obtained for $\log|\zeta_m(t)|^2$. In the $\chi < \chi_c$ case, from the results in Fig. 3(d), it is clear that the system remains unlocalized, with an IPR that undergoes small-amplitude oscillations. As already mentioned, in this case the quenched $|\psi_0(t)\rangle$ depends on the first eigenstates of $\hat{H}_1$, which are not localized in the $\hat{J}_z$ basis states and have regular energy differences between them. For $\chi > \chi_c$ the quench brings the system to higher energies, into the broken-symmetry phase of the ESQPT. In this case the dynamics of the system is controlled by higher-energy eigenstates of $\hat{H}_1$ and, for short times, eigenstates with larger energy differences modify the dynamics of the system, leading to significant oscillations at times $t < 100$ in Fig. 3(f). For longer times, more eigenstates contribute to the evolution of $|\psi_0(t)\rangle$. The energies associated with these eigenstates have a more complex spectrum than in the previous case, which explains the $I_0(t)$ irregular oscillations. The critical case, when $\chi = \chi_c$, shown in Fig. 3(e), is of special interest. The state of the system at the critical energy of the ESQPT is localized but also dynamically unstable, making the system undergo a fast and strong localization to the $n = 0$ basis state at short times, as already evinced in Fig. 3(b), followed by a fast delocalization with strongly irregular oscillations at low-$I_0(t)$ values. To further explore the ESQPT influence on the MQC spectrum, we have selected several time values, marked with vertical lines in Figs. 3(d)–3(f): $t = 0$ (red solid line), $t = 8$ (blue dashed line), $t = 16$ (green dotted line), and $t = 100$ (purple dash-dotted line). We plot in Figs. 3(g)–3(i) $I_\ell[\rho(t)]$ as a function of ℓ for the selected time values, using the same colors and line styles. The localization that occurs for $\chi = \chi_c$ is evinced in the sharp maximum for time $t = 8$ in Fig. 3(h). Another interesting feature is the difference between $I_\ell[\rho(t)]$ in Figs. 3(g) and 3(i) for $t = 100$, which can be traced back to the random oscillations in the latter case. Furthermore, Fig. 3(b) suggests that the maximum number of m_z values contributing to $|\zeta_m(t)|^2$ occurs at $\chi = \chi_c$, after the fast decay at initial times with a strong localization at $m_z = 0$. Therefore, at long times, the evolved MQC spectrum has a maximal width for $\chi \simeq \chi_c$.

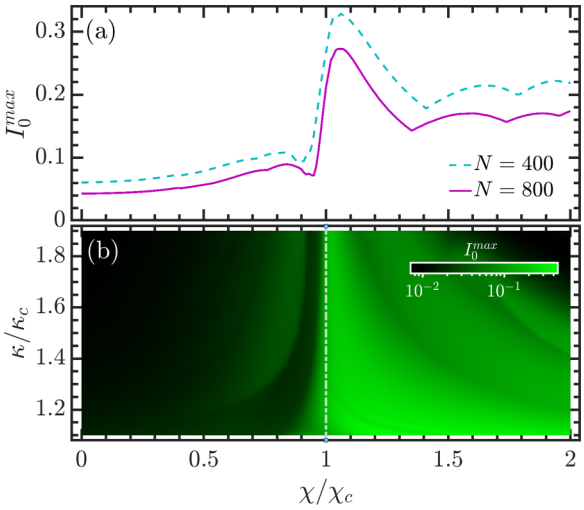

FIG. 4. (a) Maximum zero component of the MQC spectrum $I_0^{\max}$ [see Eq. (20)] as a function of χ/χ_c for a system with $\kappa = 1.5\kappa_c$, a time interval $t \in [0, \tau = 30]$, and system sizes $N = 400$ (green dashed line) and $N = 800$ (red solid line). The rapid growth of $I_0^{\max}$ near $\chi/\chi_c = 1$ indicates the presence of an ESQPT. (b) Plot of the $I_0^{\max}$ heat map as a function of χ/χ_c and κ/κ_c for a system size $N = 800$. The vertical white dash-dotted line indicates the critical line $\chi/\chi_c = 1$. The other parameters are $\kappa_c = 1/3$ and χ_c given by Eq. (14).

To make clear how to characterize ESPQTs using $I_0[\rho(t)]$, we consider the maximum value of this quantity in a time interval $[0, \tau]$, denoted by $I_0^{\max}$,

$$I_0^{\max} = \max_{t\in[0,\tau]} \{I_0[\rho(t)]\}, \quad (20)$$

where τ denotes a typical timescale for the short-term evolution of $I_0[\rho(t)]$. In the present calculation we set $\tau = 30$ and a careful check on cases with $\tau > 30$ indicates that our conclusions are still valid. In Fig. 4(a) we plot the variation of $I_0^{\max}$ with χ/χ_c for two different system sizes $N = 400, 800$ for a Hamiltonian with $\kappa = 0.5$. We clearly see that $I_0^{\max}$ undergoes an abrupt change in the neighborhood of the critical quench, independently of the system size N. As a consequence of this,

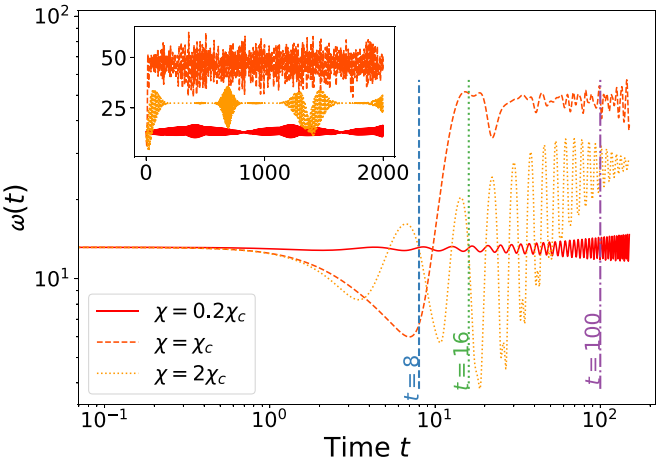

FIG. 5. Time evolution of the MQC spectrum width $w(t)$ [see Eq. (21)] on a log-log scale. From dark to light orange, $\chi/\chi_c = 0.2$ (solid line), $\chi/\chi_c = 1$ (dashed line), and $\chi/\chi_c = 2$ (dotted line), for a system with $\kappa = 1.5\kappa_c$ and size $N = 400$. The abscissa axis shares its timescale with Figs. 3(d)–3(f). In the inset the same quantity is depicted versus time using linear axes and for a longer time span. The rapid growth in the dynamics of $w(t)$ for the critical case can be traced back to the LMG ESQPT. The other parameters are $\kappa_c = 1/3$ and χ_c defined in Eq. (14).

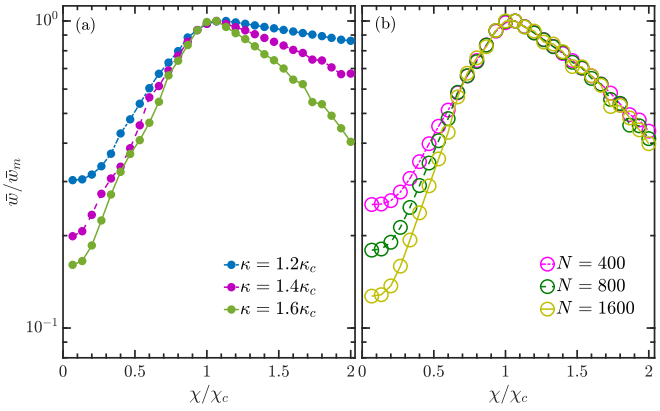

FIG. 6. Normalized long-time-averaged MQC spectrum width $\bar{w}/\bar{w}_m$, where $\bar{w}_m$ is the maximum value of $\bar{w}$, as a function of χ/χ_c for (a) several values of the κ control parameter with a system size $N = 1000$ and (b) different system size values N with $\kappa = 1.6\kappa_c$. The maximum in $\bar{w}/\bar{w}_m$ marks the presence of the ESQPT. The other parameters are $\kappa_c = 1/3$ and χ_c given by Eq. (14). All quantities plotted are dimensionless.

we suggest to use $I_0^{\max}$ to check for the existence of an ESQPT in many-body quantum systems. This is further confirmed by the results shown in Fig. 4(b), where $I_0^{\max}$ is plotted in a heat map as a function of $0 \leqslant \chi/\chi_c \leqslant 2$ and $1.1 \leqslant \kappa/\kappa_c \leqslant 1.9$ for a system size $N = 800$ and where the boundary between the system's phases is clearly located at $\chi/\chi_c \approx 1$, in good agreement with analytical results.

B. MQC spectrum width

The different amplitudes of $\zeta(t)$ shown in Figs. 3(a)–3(c) support our initial assumption that the MQC spectrum width could be a valid ESQPT probe. As we mentioned above, the MQC spectrum can be considered as an OTOC, and it is trivial to realize that its width, basically the second moment of the MQC distribution, is also a four-point correlator.

The MQC spectrum is symmetrically distributed around $\ell = 0$ and its time-dependent width is given by the second moment in Eq. (4) for $\rho(t)$ and $\hat{\mathcal{O}} = \hat{J}_z$,

$$w(t) = \Sigma[\rho(t), \hat{J}_z] = \sqrt{\sum_\ell \ell^2 I_\ell[\rho(t)]}, \tag{21}$$

which is equal to the quantum Fisher information for pure quantum states [67]. We now show that qualitative and quantitative features of $w(t)$ can be used as ESQPT checks.

Let us first consider how the dynamics of $w(t)$ is influenced by the ESQPT. This is illustrated in Fig. 5, where the time evolution of $w(t)$ for different χ/χ_c values is shown using log-log axes. Vertical lines correspond to the particular times selected in Figs. 3(d)–3(f). For $\chi = 0.2\chi_c$, before the critical quench, the width oscillates in time around its initial value (dark orange solid line). However, when the quench reaches its critical value for $\chi = \chi_c$ (light orange dashed line), we can distinguish four different regimes in the time evolution of the width $w(t)$ that are similar to the ones that have been observed with a FOTOC in chaotic models [128]: (i) an approximately constant value until $t \approx 1$, (ii) a decay to its minimum value, (iii) an exponential growth, and (iv) $w(t)$ reaches its saturation value, oscillating around it in an irregular way. The LMG is an integrable model, but the unstable stationary point in the LMG Hamiltonian, marked with a red star in Fig. 2, makes the OTOC behave as expected for chaotic systems whenever the system straddles the ESQPT critical energy [100,101]. Beyond the critical value of the quench, for $\chi > \chi_c$, the system again oscillates regularly until it reaches its saturation value, as shown for $\chi = 2\chi_c$ with the dotted light orange line in Fig. 5. In the inset we show the long-time dependence using lin-lin scale and we verify that the highest saturation value is attained for the critical quench, the one that also exhibits the highest dispersion in Fig. 3(b).

To further confirm that $w(t)$ acts as a valid ESQPT probe, we consider the long-time-averaged width, defined as

$$\bar{w} \equiv \lim_{T\to\infty} \frac{1}{T} \int_{t_0}^{t_0+T} w(t)dt. \tag{22}$$

We choose t_0 values such that $t_0 \gg 1$. In the present calculations, we set $t_0 = 10^4$ and $T = 10^3$ and we carefully check that the obtained results are the same for larger t_0 and T values.

Considering the results in Fig. 5, it is expected that $\bar{w}$ should reach its maximum $\bar{w}_m$ in the vicinity of the critical quench. This is made clear with the scaled quantity $\bar{w}/\bar{w}_m$, which is plotted as a function of $0 \leqslant \chi/\chi_c \leqslant 2$ in Fig. 6(a) for different values of κ and a fixed system size $N = 1000$ and in Fig. 6(b) for several N values and a fixed $\kappa = 1.6/3$. One can clearly appreciate that, in both cases, $\bar{w}$ has a peak around $\chi/\chi_c = 1$, regardless of the strength of the control parameter κ and the system size N, which means that $\bar{w}$ is an ESQPT precursor and the location of the peak provides a numerical estimation of the critical χ value: The peak location tends towards $\chi/\chi_c = 1$ for increasing system-size values.

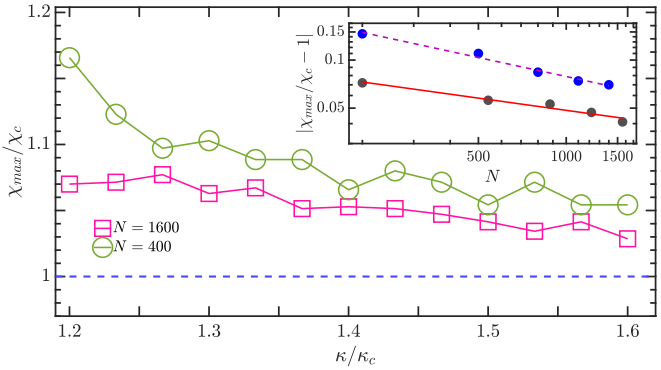

FIG. 7. Normalized quench parameter $\chi_{\max}/\chi_c$, where $\chi_{\max}$ is the quench parameter value for a maximum long-time-averaged MQC spectrum width $\bar{\omega}_m$ as a function of κ/κ_c for size values $N = 400$ and 1600. The horizontal dashed line marks the value $\chi_{\max}/\chi_c = 1$. The inset shows $|\chi_{\max}/\chi_c - 1|$ as a function of N on a log-log scale for $\kappa_1 = 1.3\kappa_c$ (blue dots) and $\kappa_1 = 1.5\kappa_c$ (gray dots). The purple dashed and red solid lines are of the form $|\chi_{\max}/\chi_c - 1| = C_\kappa N^{-\beta_\kappa}$, with $C_{\kappa_1} = 0.3952$ and $\beta_{\kappa_1} = 0.1902$ and with $C_{\kappa_2} = 0.2540$ and $\beta_{\kappa_2} = 1.273$, respectively. The other parameters are $\kappa_c = 1/3$ and χ_c obtained from Eq. (14). All quantities plotted are dimensionless.

Moreover, the variation of $\bar{w}/\bar{w}_m$ around $\chi/\chi_c = 1$ is independent of the control parameter or the value of the system size, denoting the universal character of the scaling around the critical point. This effect is particularly conspicuous in Fig. 6(b), where the values before and after the critical point are qualitatively different. This difference can be traced back to a scaling of $\bar{w}$ with N for $\chi/\chi_c < 1$ which switches to an N scaling as the system gets close to the critical point and all the way to $\chi/\chi_c = 2$. Such critical scaling of $\bar{w}/\bar{w}_m$ deserves further analysis for a detailed understanding of its underlying mechanism.

The previous results are confirmed in Fig. 7, where the χ value that corresponds to maximum $\bar{w}$, denoted by $\chi_{\max}$, is plotted as a function of κ for $N = 400$ and 1600. To better grasp how $\chi_{\max}$ tends to χ_c as N increases, we include an inset in Fig. 7 where the variation of $|\chi_{\max}/\chi_c - 1|$ with the system size N for $\kappa = 1.3/3$ and 0.5 is plotted using a log-log scale. It can be easily appreciated that, regardless of the κ value, the scaling behavior of $|\chi_{\max}/\chi_c - 1|$ is well fitted by a power law $|\chi_{\max}/\chi_c - 1| = C_\kappa N^{-\beta_\kappa}$, where C_κ and β_κ are κ-dependent quantities. Hence, $\chi_{\max} \to \chi_c$ as N goes to infinity.

C. MQC spectrum of the long-time-averaged state

We now discuss how to unveil ESQPT signatures through the MQC spectrum of the long-time-averaged state, which is defined as

$$\bar{\rho} \equiv \lim_{T\to\infty} \frac{1}{T}\int_0^T dt\, \rho(t) = \lim_{T\to\infty} \frac{1}{T}\int_0^T dt\, e^{-i\hat{H}_1 t}|\psi_0\rangle\langle\psi_0|e^{i\hat{H}_1 t}$$
$$= \sum_k |\langle\phi_k|\psi_0\rangle|^2 |\phi_k\rangle\langle\phi_k|. \tag{23}$$

In the last step we have used the closure relation $\hat{\mathbb{I}} = \sum_k |\phi_k\rangle\langle\phi_k|$, with $|\phi_k\rangle$ the kth eigenstates of $\hat{H}_1$. Moreover, the integration has been carried out considering that there is no degeneracy in the $\hat{H}_1$ energy spectrum. This assumption is valid because we start from a positive-parity state and the operator $\hat{J}_z$ does not mix different parity states. It is worth noting that $\bar{\rho}$ is a mixed state.

To calculate the MQC spectrum of $\bar{\rho}$, we first express this state in the $\hat{J}_z$ basis as

$$\bar{\rho} = \sum_\ell \bar{\rho}_\ell = \sum_\ell \sum_m \bar{\rho}_{m+\ell,m} |m+\ell\rangle\langle m|, \tag{24}$$

where

$$\bar{\rho}_{m+\ell,m} = \langle m+\ell|\bar{\rho}|m\rangle$$
$$= \sum_k \langle m+\ell|\phi_k\rangle\langle\phi_k|m\rangle|\langle\psi_0|\phi_k\rangle|^2. \tag{25}$$

Finally, the resulting ℓth component of the MQC spectrum is

$$I_\ell(\bar{\rho}) = \mathrm{Tr}(\bar{\rho}_\ell^\dagger \bar{\rho}_\ell) = \sum_m |\bar{\rho}_{m+\ell,m}|^2. \tag{26}$$

The formula (26) indicates that the MQC spectrum of $\bar{\rho}$ is determined by the dependence of $\bar{\rho}_{m+\ell,m}$ on ℓ and m. This is made clear in Fig. 8, where $\bar{\rho}_{m+\ell,m}$ is depicted as a heat map dependent on the system-size-scaled values of m and ℓ for three different values of χ/χ_c with $\kappa = 0.5$. The variation of $\bar{\rho}_{m+\ell,m}$ is shown as the system goes through the critical quench. In particular, in the $\chi/\chi_c < 1$ case, $\bar{\rho}_{m+\ell,m}$ is a smooth function deprived of nodes that extends in a wide ℓ range, as shown in Fig. 8(a). This is due to the large overlap between $|\phi_0\rangle$ and $|\psi_0\rangle$. In contrast, in the $\chi/\chi_c > 1$ phase, there are several eigenstates $|\phi_k\rangle$ for large-k values contributing to $|\psi_0\rangle$. Hence, the summation of their distributions in the basis states as in Eq. (25) is more complex, as shown in Fig. 8(c), where $\bar{\rho}_{\ell+m,m}$ oscillates with both variables due to interference effects and quickly decays to zero outside a range of $|\ell|$ and m values. As illustrated in Fig. 8(b), at the critical value $\chi/\chi_c = 1$, $\bar{\rho}_{m+\ell,m}$ displays a dependence on ℓ and m that differs from the two cases previously described. It again exhibits a complex oscillating pattern as in previous case, but the oscillations extend along large-m and -ℓ ranges. In addition to this, the most salient feature is the strong localization in the $n = 0$ state. The results for the critical case can be understood from the critical character of this state and the divergence of the density of states at the ESQPT critical energy, which makes $|\psi_0\rangle$ become a highly localized state in the $\hat{J}_z$ basis.

It is clear from the heat maps of $\bar{\rho}_{m+\ell,m}$ in Figs. 8(a)–(c) that the model ESQPT shapes the MQC spectrum. This is indeed confirmed in Fig. 9(a), where we depict the MQC spectrum $I_\ell(\bar{\rho})$ as a heat map depending on ℓ and χ/χ_c for the $\kappa = 0.5$ case. In this figure it is clear how, for increasing χ/χ_c values, the ℓ range associated with large $I_\ell(\bar{\rho})$ exhibits a rapid decrease as χ passes through the critical value. Moreover, the higher values of $\bar{\rho}_{m+\ell,m}$ for the $\chi/\chi_c < 1$ case shown in Fig. 8(a) explain the large amplitudes of the MQC spectrum in Fig. 9(a). This is clearly shown in Fig. 9(b), where the MQC spectrum for several χ/χ_c values is plotted.

The results in Figs. 9(a) and 9(b) confirm the $\bar{\rho}$ MQC spectrum as a valid candidate for an ESQPT indicator in the many-body quantum system. To further demonstrate

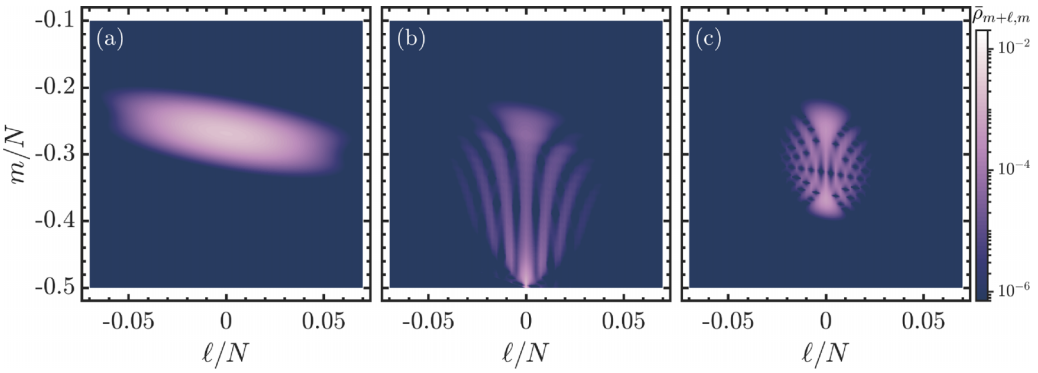

FIG. 8. Heat map of $\bar{\rho}_{m+\ell,m}$ in Eq. (25) as a function of ℓ/N and m/N for (a) $\chi/\chi_c = 0.2$, (b) $\chi/\chi_c = 1$, and (c) $\chi/\chi_c = 2$. In the three cases $N = 800$ and $\kappa = 1.5\kappa_c$, with $\kappa_c = 1/3$, while the value of χ_c is given by Eq. (14). All quantities depicted are dimensionless.

the usefulness of the MQC distribution of $\bar{\rho}$ for ESQPT characterization, we now focus on the $I_\ell(\bar{\rho})$ zero mode, denoted by $I_0(\bar{\rho})$,

$$I_0(\bar{\rho}) = \sum_m |\bar{\rho}_{m,m}|^2, \tag{27}$$

where $\bar{\rho}_{m,m} = \sum_k |\langle m|\phi_k\rangle|^2 |\langle \psi_0|\phi_k\rangle|^2$.

Figure 9(c) is a heat map for $I_0(\bar{\rho})$ as a function of the parameters κ and χ where the value of $I_0(\bar{\rho})$ exhibits a local maximum at the critical quench value $\chi/\chi_c = 1$. This is even more evident in Fig. 9(d), where the dependence of $I_0(\bar{\rho})$ on χ/χ_c for several κ values (see the legend) is depicted. Hence, the zero mode of the $\bar{\rho}$ MQC spectrum is sensitive to the presence of the ESQPT. The local maximum of $I_0(\bar{\rho})$ at $\chi/\chi_c = 1$ can be explained by the strong localization in the $n = 0$ basis state and the large range of m values contributing to $I_0(\bar{\rho})$, as shown in Fig. 8(b). To further understand this behavior, we could consider a simpler system, where the quench Hamiltonian is $\hat{H}(\kappa = 0) \propto \hat{J}_z$. In this case, the population of the MQC spectrum for a long-time average state would coincide with the long-time average of the Loschmidt echo (see Refs. [49,51]). This explains the similarities between Fig. 9(d) herein and Fig. 5(d) of Ref. [51], where Wang and Quan found a comparable behavior for the long-time average of the Loschmidt echo. With this setup, the higher the localization in the eigenbasis of the quench Hamiltonian, the larger the value of $I_0(\bar{\rho})$. A similar phenomenology is observed in our system. Looking at Fig. 8, we realize that $I_0(\bar{\rho})$ in Fig. 9(d) is higher when the state is well localized in the quench eigenbasis.

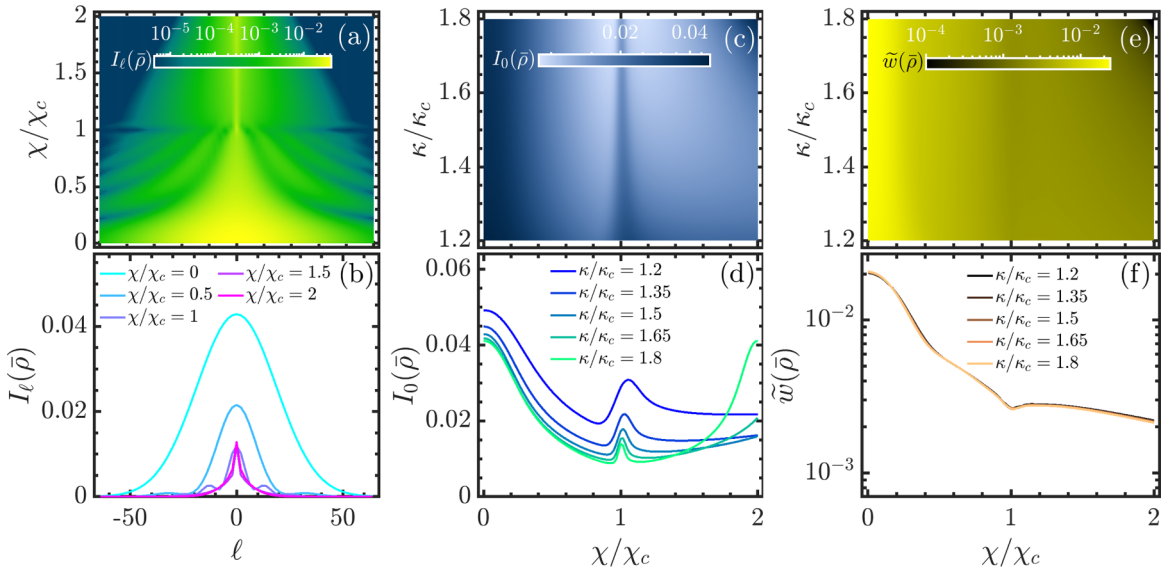

FIG. 9. (a) Heat map of the long-time-averaged state MQC spectrum $I_\ell(\bar{\rho})$ defined in Eq. (26) as a function of ℓ and χ/χ_c for $\kappa = 1.5\kappa_c$. (b) Plot of $I_\ell(\bar{\rho})$ as a function of ℓ for several values of the quench parameter χ/χ_c (see the legend) with $\kappa = 1.5\kappa_c$. The crossing of the ESQPT drives a significant change in the MQC spectrum. (c) Heat map of the zero component of the long-time-averaged state MQC spectrum $I_0(\bar{\rho})$ [see Eq. (27)] as a function of χ/χ_c and κ/κ_c. (d) Plot of $I_0(\bar{\rho})$ as a function of χ/χ_c for selected values of κ/κ_c (see the legend). (e) Heat map of the size-scaled width of the long-time-averaged state MQC spectrum $\tilde{w}(\bar{\rho}) = w(\bar{\rho})/N$ as a function of χ/χ_c and κ/κ_c. (f) Plot of $\tilde{w}(\bar{\rho})$ as a function of χ/χ_c for several values of κ/κ_c (see the legend). In (c)–(f) the local maximum in $I_0(\bar{\rho})$ and the local minimum in $w(\bar{\rho})/N$ make these two quantities possible ESQPT probes. In all panels $N = 2j = 800$, $\kappa_c = 1/3$, and χ_c is obtained from Eq. (14). All quantities depicted are dimensionless.

Furthermore, as the MQC spectrum has a different width in the two ESQPT phases, the $\bar{\rho}$ MQC spectrum width should also change due to the presence of the ESQPT. To verify this point, we show in Fig. 9(e) the scaled width of the $\bar{\rho}$ MQC spectrum $\tilde{w}(\bar{\rho}) = w(\bar{\rho})/N$ as a function of κ and χ. It is clear that $\tilde{w}$ has a kink at the critical point, regardless of the κ value, in contrast to the case of long-time-averaged $w(t)$, which exhibits a maximum in the neighborhood of the critical point, as seen in Fig. 6. The kink in $w(\bar{\rho})/N$ is clearly appreciated in Fig. 9(f), where this quantity is depicted as a function of χ/χ_c for several κ values, and it can be traced back to the low-$\bar{\rho}_{m+\ell,m}$ values at the critical point [cf. Fig. 8(b)]. Finally, it is important to appreciate that the evolution of $w(\bar{\rho})/N$ as a function of χ/χ_c is basically independent of the κ value.

V. CONCLUSION

In the present article we have investigated, through the MQC spectrum, the influence on quantum coherence of the LMG model ESQPT, a logarithmic divergence in the mean-field limit of the density of states. By using a sudden-quench protocol and expanding the evolved state in the $\hat{J}_z$ quasispin basis, we have found that the underlying ESQPT has a strong impact on the time evolution of the MQC spectrum, whose temporal dependence at the quench critical parameter value is a reliable indicator of the presence of an ESQPT. The time evolution of the MQC spectrum can be understood by studying the $\zeta(t)$ coefficients defined in Eq. (17). In particular, the system gets quickly localized in the $\hat{J}_z$ basis state with a minimum value of m_z at the critical value of the quench parameter. We have also shown that this localization leads to a clear maximum at short times in the zero-mode MCQ spectrum $I_{\ell=0}$ followed by a high dispersion [see Fig. 3(e)].

A high dispersion is also observed when we study the MQC spectrum versus the differences ℓ. To understand this behavior, we plotted the width of the distribution and identified different ways for the system to reach saturation. In particular, in the quench to the critical energy of the ESQPT case, we observe regimes previously identified in other OTOCs and a maximal saturation value. Another result of interest in the critical quench is that the long-time saturation width peaks at locations that tend to the critical point for increasing system sizes.

We have also analyzed the properties of the MQC distribution for the long-time-averaged state, which is defined as the long-time average of the evolved state [cf. Eq. (23)], and we have observed that the ESQPT is responsible for an abrupt change in the MQC spectrum of the long-time-averaged state. Moreover, its zero mode and width also stand as good detectors of the ESQPT in the LMG model. The first one is maximum and the second minimum when the quench parameter reaches its critical value.

The present work focused on the LMG model, but our conclusions are a consequence of the nature of the ESQPT in this model, characterized by a logarithmic divergence of the density of states at a certain excited energy. As explained, despite its simplicity, the LMG model has proved a suitable platform to study GSQPTs, ESQPTs, and other critical phenomena. Furthermore, there are several experimental realizations of this model and the connection between the MQC spectrum and a FOTOC [cf. Eq. (3)] allows for the experimental access to the MQC spectrum through protocols that could be implemented in different platforms [66,68] and do not require full quantum state tomography at each time. Based on these facts, we expect that our results may motivate further experimental efforts to investigate ESQPTs using the MQC spectrum. In fact, ESQPTs akin to the one in the LMG model appear in many other models with a single effective degree of freedom and therefore our findings will also apply for other systems that undergo the same kind of ESQPT as the LMG model. A natural extension of the present work is a systematic exploration of the ESQPT effects on the MQC spectrum in other quantum many-body systems.

ACKNOWLEDGMENTS

Q.W. acknowledges support from the Slovenian Research and Innovation Agency under Grants No. J1-4387 and No. P1-0306, National Science Foundation of China under Grant No. 11805165, and Zhejiang Provincial Nature Science Foundation under Grant No. LY20A050001. This project has also received funding from Grant No. PID2022-136228NB-C21 funded by MICIU/AEI/10.13039/501100011033 and, as appropriate, by ERDF, A way of making Europe, by ERDF/EU, by the European Union or by the European Union NextGenerationEU/PRTR, and by the FEDER-UHU project POSH-AI, Project No. EPIT1462023. J.K.-R. also acknowledges support from a Spanish Ministerio de Universidades Margarita Salas Fellowship. Computing resources supporting this work were partly provided by the CEAFMC and Universidad de Huelva High Performance Computer located at the Campus Universitario el Carmen and funded by FEDER/MINECO Project No. UNHU-15CE-2848.

[1] S. Sachdev, Phys. World **12**, 33 (1999).
[2] L. Carr, *Understanding Quantum Phase Transitions* (CRC, Boca Raton, 2010).
[3] P. Cejnar, M. Macek, S. Heinze, J. Jolie, and J. Dobeš, J. Phys. A: Math. Gen. **39**, L515 (2006).
[4] P. Cejnar and P. Stránský, Phys. Rev. E **78**, 031130 (2008).
[5] M. Caprio, P. Cejnar, and F. Iachello, Ann. Phys. (NY) **323**, 1106 (2008).
[6] P. Cejnar, P. Stránský, M. Macek, and M. Kloc, J. Phys. A: Math. Theor. **54**, 133001 (2021).
[7] P. Stránský and P. Cejnar, Phys. Lett. A **380**, 2637 (2016).
[8] F. Leyvraz and W. D. Heiss, Phys. Rev. Lett. **95**, 050402 (2005).
[9] G. Engelhardt, V. M. Bastidas, W. Kopylov, and T. Brandes, Phys. Rev. A **91**, 013631 (2015).
[10] M. Šindelka, L. F. Santos, and N. Moiseyev, Phys. Rev. A **95**, 010103(R) (2017).

[11] L. F. Santos, M. Távora, and F. Pérez-Bernal, Phys. Rev. A **94**, 012113 (2016).
[12] D. J. Nader, C. A. González-Rodríguez, and S. Lerma-Hernández, Phys. Rev. E **104**, 064116 (2021).
[13] J. Gamito, J. Khalouf-Rivera, J. M. Arias, P. Pérez-Fernández, and F. Pérez-Bernal, Phys. Rev. E **106**, 044125 (2022).
[14] M. A. Bastarrachea-Magnani, S. Lerma-Hernández, and J. G. Hirsch, Phys. Rev. A **89**, 032101 (2014).
[15] P. Pérez-Fernández, P. Cejnar, J. M. Arias, J. Dukelsky, J. E. García-Ramos, and A. Relaño, Phys. Rev. A **83**, 033802 (2011).
[16] T. Brandes, Phys. Rev. E **88**, 032133 (2013).
[17] R. Puebla, A. Relaño, and J. Retamosa, Phys. Rev. A **87**, 023819 (2013).
[18] P. Pérez-Fernández and A. Relaño, Phys. Rev. E **96**, 012121 (2017).
[19] R. Puebla, M.-J. Hwang, and M. B. Plenio, Phys. Rev. A **94**, 023835 (2016).
[20] P. Feldmann, C. Klempt, A. Smerzi, L. Santos, and M. Gessner, Phys. Rev. Lett. **126**, 230602 (2021).
[21] J. Cabedo and A. Celi, Phys. Rev. Res. **3**, 043215 (2021).
[22] Z.-X. Niu and Q. Wang, Phys. Rev. E **110**, 064112 (2024).
[23] B. Meyer-Hoppe, F. Anders, P. Feldmann, L. Santos, and C. Klempt, Phys. Rev. Lett. **131**, 243402 (2023).
[24] D. Larese and F. Iachello, J. Mol. Struct. **1006**, 611 (2011).
[25] D. Larese, F. Pérez-Bernal, and F. Iachello, J. Mol. Struct. **1051**, 310 (2013).
[26] J. Khalouf-Rivera, F. Pérez-Bernal, and M. Carvajal, J. Quant. Spectrosc. Radiat. Transfer **261**, 107436 (2021).
[27] J. Khalouf-Rivera, M. Carvajal, and F. Pérez-Bernal, SciPost Phys. **12**, 002 (2022).
[28] J. Khalouf-Rivera, M. Carvajal, L. Santos, and F. Pérez-Bernal, J. Phys. Chem. A **123**, 9544 (2019).
[29] J. Khalouf-Rivera, F. Pérez-Bernal, and M. Carvajal, Phys. Rev. A **105**, 032215 (2022).
[30] J. Khalouf-Rivera, Q. Wang, L. F. Santos, J.-E. García-Ramos, M. Carvajal, and F. Pérez-Bernal, Phys. Rev. A **109**, 062219 (2024).
[31] V. M. Bastidas, P. Pérez-Fernández, M. Vogl, and T. Brandes, Phys. Rev. Lett. **112**, 140408 (2014).
[32] I. García-Mata, E. Vergini, and D. A. Wisniacki, Phys. Rev. E **104**, L062202 (2021).
[33] M. Macek, P. Stránský, A. Leviatan, and P. Cejnar, Phys. Rev. C **99**, 064323 (2019).
[34] W.-T. Dong, Y. Zhang, B.-C. He, F. Pan, Y.-A. Luo, J. P. Draayer, and S. Karampagia, J. Phys. G **48**, 045103 (2021).
[35] Q. Wang and F. Pérez-Bernal, Phys. Rev. E **104**, 034119 (2021).
[36] D. Mondal, S. Sinha, and S. Sinha, Phys. Rev. E **105**, 014130 (2022).
[37] Q.-W. Wang and S. Wu, Phys. Rev. A **102**, 063531 (2020).
[38] J. Chávez-Carlos, T. L. M. Lezama, R. G. Cortiñas, J. Venkatraman, M. H. Devoret, V. S. Batista, F. Pérez-Bernal, and L. F. Santos, npj Quantum Inf. **9**, 76 (2023).
[39] M. A. P. Reynoso, D. J. Nader, J. Chávez-Carlos, B. E. Ordaz-Mendoza, R. G. Cortiñas, V. S. Batista, S. Lerma-Hernández, F. Pérez-Bernal, and L. F. Santos, Phys. Rev. A **108**, 033709 (2023).
[40] F. Iachello, R. G. Cortiñas, F. Pérez-Bernal, and L. F. Santos, J. Phys. A: Math. Theor. **56**, 495305 (2023).
[41] L. F. Santos and F. Pérez-Bernal, Phys. Rev. A **92**, 050101(R) (2015).
[42] P. Cejnar and P. Stránský, Phys. Lett. A **381**, 984 (2017).
[43] A. Relaño, Phys. Rev. Lett. **121**, 030602 (2018).
[44] A. Relaño, J. M. Arias, J. Dukelsky, J. E. García-Ramos, and P. Pérez-Fernández, Phys. Rev. A **78**, 060102(R) (2008).
[45] M. Kloc, P. Stránský, and P. Cejnar, Phys. Rev. A **98**, 013836 (2018).
[46] Q. Wang and F. Pérez-Bernal, Phys. Rev. A **100**, 062113 (2019).
[47] P. Stránský, P. Cejnar, and R. Filip, Phys. Rev. A **104**, 053722 (2021).
[48] M. Kloc, D. Šimsa, F. Hanák, P. R. Kaprálová-Žďánská, P. Stránský, and P. Cejnar, Phys. Rev. A **103**, 032213 (2021).
[49] J. Khalouf-Rivera, J. Gamito, F. Pérez-Bernal, J. M. Arias, and P. Pérez-Fernández, Phys. Rev. E **107**, 064134 (2023).
[50] R. Puebla and A. Relaño, Phys. Rev. E **92**, 012101 (2015).
[51] Q. Wang and H. T. Quan, Phys. Rev. E **96**, 032142 (2017).
[52] Z. Mzaouali, R. Puebla, J. Goold, M. El Baz, and S. Campbell, Phys. Rev. E **103**, 032145 (2021).
[53] W. Kopylov and T. Brandes, New J. Phys. **17**, 103031 (2015).
[54] A. Rubio-García, A. L. Corps, A. Relaño, R. A. Molina, F. Pérez-Bernal, J. E. García-Ramos, and J. Dukelsky, Phys. Rev. A **106**, L010201 (2022).
[55] A. Streltsov, G. Adesso, and M. B. Plenio, Rev. Mod. Phys. **89**, 041003 (2017).
[56] J. Baum, M. Munowitz, A. N. Garroway, and A. Pines, J. Chem. Phys. **83**, 2015 (1985).
[57] J. Baum and A. Pines, J. Am. Chem. Soc. **108**, 7447 (1986).
[58] J. Keeler, *Understanding NMR Spectroscopy* (Wiley, New York, 2011).
[59] P. Cappellaro, in *Quantum State Transfer and Network Engineering*, edited by G. M. Nikolopoulos and I. Jex (Springer, Berlin, 2014), pp. 183–222.
[60] K. Macieszczak, E. Levi, T. Macrì, I. Lesanovsky, and J. P. Garrahan, Phys. Rev. A **99**, 052354 (2019).
[61] M. Munowitz, A. Pines, and M. Mehring, J. Chem. Phys. **86**, 3172 (1987).
[62] C. M. Sánchez, R. H. Acosta, P. R. Levstein, H. M. Pastawski, and A. K. Chattah, Phys. Rev. A **90**, 042122 (2014).
[63] S. I. Doronin, Phys. Rev. A **68**, 052306 (2003).
[64] G. B. Furman, V. M. Meerovich, and V. L. Sokolovsky, Phys. Rev. A **78**, 042301 (2008).
[65] E. B. Fel'dman, A. N. Pyrkov, and A. I. Zenchuk, Philos. Trans. R. Soc. A **370**, 4690 (2012).
[66] M. Gärttner, J. G. Bohnet, A. Safavi-Naini, M. L. Wall, J. J. Bollinger, and A. M. Rey, Nat. Phys. **13**, 781 (2017).
[67] M. Gärttner, P. Hauke, and A. M. Rey, Phys. Rev. Lett. **120**, 040402 (2018).
[68] R. J. Lewis-Swan, S. R. Muleady, and A. M. Rey, Phys. Rev. Lett. **125**, 240605 (2020).
[69] F. Deng, P. Xu, S. Yi, and W. Zhang, Commun. Theor. Phys. **76**, 015501 (2024).
[70] D. P. Pires and T. Macrì, Phys. Rev. B **104**, 155141 (2021).
[71] G. A. Álvarez and D. Suter, Phys. Rev. Lett. **104**, 230403 (2010).
[72] G. A. Álvarez, D. Suter, and R. Kaiser, Science **349**, 846 (2015).

[73] K. X. Wei, C. Ramanathan, and P. Cappellaro, Phys. Rev. Lett. **120**, 070501 (2018).

[74] H. Lipkin, N. Meshkov, and A. Glick, Nucl. Phys. **62**, 188 (1965).

[75] N. Meshkov, A. Glick, and H. Lipkin, Nucl. Phys. **62**, 199 (1965).

[76] A. Glick, H. Lipkin, and N. Meshkov, Nucl. Phys. **62**, 211 (1965).

[77] N. Defenu, T. Enss, M. Kastner, and G. Morigi, Phys. Rev. Lett. **121**, 240403 (2018).

[78] J. Lang, B. Frank, and J. C. Halimeh, Phys. Rev. Lett. **121**, 130603 (2018).

[79] Á. L. Corps and A. Relaño, Phys. Rev. Lett. **130**, 100402 (2023).

[80] R. Botet and R. Jullien, Phys. Rev. B **28**, 3955 (1983).

[81] S. Dusuel and J. Vidal, Phys. Rev. Lett. **93**, 237204 (2004).

[82] P. Ribeiro, J. Vidal, and R. Mosseri, Phys. Rev. Lett. **99**, 050402 (2007).

[83] P. Titum and M. F. Maghrebi, Phys. Rev. Lett. **125**, 040602 (2020).

[84] S. Campbell, Phys. Rev. B **94**, 184403 (2016).

[85] Y.-H. Ma, S.-H. Su, and C.-P. Sun, Phys. Rev. E **96**, 022143 (2017).

[86] A. U. C. Hardal, M. Paternostro, and O. E. Müstecaplıoğlu, Phys. Rev. E **97**, 042127 (2018).

[87] Z.-Z. Zhang and W. Wu, Phys. Rev. E **106**, 034104 (2022).

[88] G. Salvatori, A. Mandarino, and M. G. A. Paris, Phys. Rev. A **90**, 022111 (2014).

[89] Q. Guan and R. J. Lewis-Swan, Phys. Rev. Res. **3**, 033199 (2021).

[90] L. Garbe, O. Abah, S. Felicetti, and R. Puebla, Quantum Sci. Technol. **7**, 035010 (2022).

[91] T. Caneva, R. Fazio, and G. E. Santoro, Phys. Rev. B **78**, 104426 (2008).

[92] R. Puebla, S. Deffner, and S. Campbell, Phys. Rev. Res. **2**, 032020(R) (2020).

[93] O. Abah, G. De Chiara, M. Paternostro, and R. Puebla, Phys. Rev. Res. **4**, L022017 (2022).

[94] J. Vidal, S. Dusuel, and T. Barthel, J. Stat. Mech. (2007) P01015.

[95] J. Wilms, J. Vidal, F. Verstraete, and S. Dusuel, J. Stat. Mech. (2012) P01023.

[96] G. D. Chiara and A. Sanpera, Rep. Prog. Phys. **81**, 074002 (2018).

[97] J. Bao, B. Guo, H.-G. Cheng, M. Zhou, J. Fu, Y.-C. Deng, and Z.-Y. Sun, Phys. Rev. A **101**, 012110 (2020).

[98] M.-L. Hu, F. Fang, and H. Fan, Phys. Rev. A **104**, 062416 (2021).

[99] J. Bao, Y.-H. Liu, and B. Guo, J. Phys.: Condens. Matter **33**, 495401 (2021).

[100] S. Pilatowsky-Cameo, J. Chávez-Carlos, M. A. Bastarrachea-Magnani, P. Stránský, S. Lerma-Hernández, L. F. Santos, and J. G. Hirsch, Phys. Rev. E **101**, 010202(R) (2020).

[101] T. Xu, T. Scaffidi, and X. Cao, Phys. Rev. Lett. **124**, 140602 (2020).

[102] K. Pal, K. Pal, and T. Sarkar, Phys. Rev. E **107**, 044130 (2023).

[103] A. Russomanno, F. Iemini, M. Dalmonte, and R. Fazio, Phys. Rev. B **95**, 214307 (2017).

[104] Á. Sáiz, J. Khalouf-Rivera, J. M. Arias, P. Pérez-Fernández, and J. Casado-Pascual, Quantum **8**, 1365 (2024).

[105] M. Albiez, R. Gati, J. Fölling, S. Hunsmann, M. Cristiani, and M. K. Oberthaler, Phys. Rev. Lett. **95**, 010402 (2005).

[106] T. Zibold, E. Nicklas, C. Gross, and M. K. Oberthaler, Phys. Rev. Lett. **105**, 204101 (2010).

[107] A. G. Araujo-Ferreira, R. Auccaise, R. S. Sarthour, I. S. Oliveira, T. J. Bonagamba, and I. Roditi, Phys. Rev. A **87**, 053605 (2013).

[108] P. Jurcevic, B. P. Lanyon, P. Hauke, C. Hempel, P. Zoller, R. Blatt, and C. F. Roos, Nature (London) **511**, 202 (2014).

[109] P. Jurcevic, H. Shen, P. Hauke, C. Maier, T. Brydges, C. Hempel, B. P. Lanyon, M. Heyl, R. Blatt, and C. F. Roos, Phys. Rev. Lett. **119**, 080501 (2017).

[110] J. Zhang, G. Pagano, P. W. Hess, A. Kyprianidis, P. Becker, H. Kaplan, A. V. Gorshkov, Z.-X. Gong, and C. Monroe, Nature (London) **551**, 601 (2017).

[111] V. Makhalov, T. Satoor, A. Evrard, T. Chalopin, R. Lopes, and S. Nascimbene, Phys. Rev. Lett. **123**, 120601 (2019).

[112] J. A. Muniz, D. Barberena, R. J. Lewis-Swan, D. J. Young, J. R. K. Cline, A. M. Rey, and J. K. Thompson, Nature (London) **580**, 602 (2020).

[113] K. Xu, Z.-H. Sun, W. Liu, Y.-R. Zhang, H. Li, H. Dong, W. Ren, P. Zhang, F. Nori, D. Zheng, H. Fan, and H. Wang, Sci. Adv. **6**, eaba4935 (2020).

[114] M. J. Cervia, A. B. Balantekin, S. N. Coppersmith, C. W. Johnson, P. J. Love, C. Poole, K. Robbins, and M. Saffman, Phys. Rev. C **104**, 024305 (2021).

[115] M. Q. Hlatshwayo, Y. Zhang, H. Wibowo, R. LaRose, D. Lacroix, and E. Litvinova, Phys. Rev. C **106**, 024319 (2022).

[116] Z. Li, S. Colombo, C. Shu, G. Vélez, S. Pilatowsky-Cameo, R. Schmied, S. Choi, M. Lukin, E. Pedrozo-Peñafiel, and V. Vuletic, Science **380**, 1381 (2023).

[117] S. Lacelle, Adv. Magn. Opt. Reson. **16**, 173 (1991).

[118] E. B. Fel'dman and A. N. Pyrkov, JETP Lett. **88**, 398 (2008).

[119] R. J. Lewis-Swan, A. Safavi-Naini, J. J. Bollinger, and A. M. Rey, Nat. Commun. **10**, 1581 (2019).

[120] H. Shen, P. Zhang, R. Fan, and H. Zhai, Phys. Rev. B **96**, 054503 (2017).

[121] S. Dusuel and J. Vidal, Phys. Rev. B **71**, 224420 (2005).

[122] E. Romera, M. Calixto, and O. Castaños, Phys. Scr. **89**, 095103 (2014).

[123] D. Gutiérrez-Ruiz, D. Gonzalez, J. Chávez-Carlos, J. G. Hirsch, and J. D. Vergara, Phys. Rev. B **103**, 174104 (2021).

[124] P. Pérez-Fernández, A. Relaño, J. M. Arias, J. Dukelsky, and J. E. García-Ramos, Phys. Rev. A **80**, 032111 (2009).

[125] J. M. Radcliffe, J. Phys. A: Gen. Phys. **4**, 313 (1971).

[126] W.-M. Zhang, D. H. Feng, and R. Gilmore, Rev. Mod. Phys. **62**, 867 (1990).

[127] M. C. Gutzwiller, *Chaos in Classical and Quantum Mechanics*, Interdisciplinary Applied Mathematics Vol. 1 (Springer, New York, 2013).

[128] J. Chávez-Carlos, B. López-del-Carpio, M. A. Bastarrachea-Magnani, P. Stránský, S. Lerma-Hernández, L. F. Santos, and J. G. Hirsch, Phys. Rev. Lett. **122**, 024101 (2019).